Supplementary Materials for

3D fault architecture controls the dynamism of earthquake swarms

Zachary E. Ross*, Elizabeth S. Cochran, Daniel T. Trugman, Jonathan D. Smith

*Corresponding author. Email: zross@caltech.edu

This PDF file includes:

Materials and Methods
Figs. S1 to S6
References

Materials and Methods

Data

We used several types of data in this study. First, we used continuous waveforms from the Southern California Seismic Network (SCSN), which are publicly available from the Southern California Earthquake Data Center (scedc.caltech.edu). Specifically, we used 38 continuous stations within 100 km of the Cahuilla swarm (Figure S1) for the period 2016-01-01 to 2019-06-28. Only EH and HH channels were processed. All seismicity data were produced for this study from scratch, starting from the raw continuous data. The focal mechanisms shown in the figures were determined by SCSN.

To build a training dataset for the deep neural networks, we used the event waveforms for all earthquakes listed in the SCSN catalog from 2000-2017. We also used publicly available phase data provided by the SCSN for the same period. These phase picks have been manually reviewed.

Seismicity catalog construction

We used deep learning methods to build our seismicity catalog by detecting and locating earthquakes over the entire continuous waveform dataset. The procedure first uses the generalized phase detection approach (*39*) to perform single station phase detection on all 3-component stations and then associates these detections across the seismic network to specific event detections.

For the phase detection, we built a training dataset of 1 million P-wave and S-wave seismograms from southern California. The datasets were assembled by randomly selecting 1 million P- and S-wave picks each from the SCSN archives (see Data), along with their associated 3-component seismograms. The seismograms were 16 seconds long, with the pick randomly located somewhere within the 16 second window. The data were filtered between 1-20 Hz for this part of the procedure.

The neural network uses a U-net architecture (*40*) to predict a binary segmentation mask 0.2 sec in duration, centered on the real picks, which was motivated by the segmentation network of (*41*) that uses DeepLab v3+. The model was trained using the Adam optimization algorithm (*42*) with default parameters and early stopping criteria. Picks were made by taking the peak sigmoid probability whenever a value of 0.5 was exceeded for either phase type. The trained model was applied to all continuous waveform data to build a database of tentative phase arrivals. In total, 37 million phase detections were made.

Next, we applied the PhaseLink algorithm (*43*) to associate the phase detections to earthquakes and build an initial catalog. PhaseLink is a deep learning algorithm for phase association and uses Gated Recurrent Units to sequentially predict and link together phase detections. A synthetic training dataset was created for the region shown in Fig S1 by placing hypocenters randomly throughout the region. This procedure is described in detail in Ross et al. (*43*). We processed windows of 500 picks at a time with a maximum sequence duration of 120 sec. We required 12 phase detections to nucleate a cluster, merged clusters with at least 1 phase detection in common, and required a minimum of 12 detections left after removing duplicates to save an event detection. These parameters were chosen to ensure the detections were of very high quality and also to keep the false positive rate well below 1%, which was performed by visual inspection of random detections. In total 22,700 events were detected.

The detected events were then located with NonLinLoc, a probabilistic non-linear hypocenter inversion algorithm (*44*) (Fig. S3, upper panel). We used the 1D velocity model of

Hadley and Kanamori (*45*) and equal differential time likelihood function. The results were refined using station correction factors from the mean residuals over all events. Local magnitudes were estimated using the waveform processing workflow, attenuation relations, and station terms used by the Southern California Seismic Network (*46*). The calculated local magnitudes range from -0.27 to 4.56. We use a goodness of fit test at the 95% level (*47*) to estimate the magnitude of completeness of 0.56 and a b-value of 1.05. The local magnitude range for this dataset corresponds to a moment magnitude range of 0.7 to 4.4.

We then cross-correlated the earthquakes to measure precise differential times for relocation purposes. We used seismograms starting 0.1 sec before all picked phases and lasting a total of 1.0 seconds. For each earthquake, we correlated it with the 200 nearest neighbors. We required a minimum cross-correlation coefficient of 0.8 and band-pass filtered the data between 1 and 15 Hz beforehand. This resulted in 89 million differential times.

Finally, the catalog was relocated with GrowClust (*48*), a cluster-based double-difference relocation algorithm. We used a minimum *r* value of 0.82 and required at least 10 differential times for relocation. We performed 100 bootstrap resamples to estimate location errors. To prevent any potential issues from cluster splitting, we lowered the minimum connectivity fraction (0.0001) until all events in the swarm were joined into a single cluster. This final catalog is shown in Figure S3.

It should be noted that the entire catalog is an automated product; none of the detections, phase picks, or differential times have been manually refined. We did however randomly inspect many detections and picks while running the detection pipeline to ensure quality control. During this process we adjusted parameters as necessary, with the final best parameter set listed above.

Stress drop estimation

We use the spectral decomposition technique detailed in (*49*) to estimate Brune-type stress drops for a well-recorded subset of full event catalog. Spectral decomposition is an iterative inversion technique that takes as input a vector containing observed displacement spectra in log-units from many earthquakes recorded at many stations, and solves for relative source, station, and path terms at each frequency point. We apply a multitaper approach to compute P-wave spectra on vertical component channels from time windows that are 1.5 s in length, beginning 0.1 s before the phase arrival. In the inversion, we only consider spectra from that have signal-to-noise (SNR) ratio of 3.0 in the 3-30Hz frequency band. We further exclude events that have local magnitude less than 0.5 or have fewer than 6 spectral recordings that meet the SNR criteria. We also implement an automated procedure to screen for and exclude spectra from clipped waveforms, which are few in number but are sometimes observed on broadband recordings of the larger events.

Spectral decomposition is effective in isolating the relative shapes of the source spectrum, but to calculate stress drop, we first need to apply an empirical correction to remove path and station effects that are common to all sources, such as average near-source and near-station attenuation. We use the approach of (*49*) to do this, which assumes that on average, the source spectra in waveform dataset conform to the Brune model with f^{-2} falloff (*50*), but makes no assumptions regarding self-similarity. With the corrected source spectra in hand, we estimate corner frequency f_c and compute stress drop using the usual relation:

$$\Delta\sigma = \frac{7}{16} M_0 \left(\frac{f_c}{k\beta}\right)^3,$$

where M_0 is the estimated seismic moment (which is proportional to the low-frequency spectral moment), β is the shear wavespeed, which we assume to be depth-dependent and estimate from

the 1D velocity model, and k=0.38 is a model-dependent constant (*51*) that has a significant impact on the absolute level of stress drop but not the local variability, which is our focus in this work. We obtain measurement uncertainties for the stress drop of each event by bootstrapping the set of stations that go into the source spectral measurements, obtaining median values (1-sigma) of 0.15 in log10 MPa units. In total, we obtain stress drop estimates for 3041 events in the main cluster of the Cahuilla swarm (Figure S2).

Permeability estimation
The migration of seismicity has been used to estimate the permeability of rocks at depth (*27, 52, 53*). Figure S4 shows the radial distance of seismicity relative to the inferred injection point along with several diffusivity curves following $r = \sqrt{4Dt}$ (*53*). First, we note that the spatiotemporal evolution of this sequence is not, in fact, well-characterized by a square-root of time function described by this simple diffusion model. The lack of an adequate fit to a simple diffusion model are suggestive of diffusivities that vary in time due to spatial differences in the permeability of the rock. Nonetheless, these curves still provide some context for the order of magnitude of the permeability of the fault zone. The values of D = 0.005, 0.01 and 0.05 m²/s are shown in Figure S4. Over a duration of 120 days, the radial extent of the swarm grows to 3500 m, giving a diffusivity of 0.03 m²/s. The fracture permeability can then be estimated from the diffusivity by:

$$k = D\mu\left[\phi\beta_f + (1-\phi)\beta_r\right]$$

where μ is the viscosity of fluid, ϕ is the porosity, β_f and β_r are the compressibilities of water and rocks, respectively. We typical values of, $\mu = 10^{-4}$ Pa s for the viscosity of fluids at 8 km depth, $\phi = 3 \times 10^{-3}$, $\beta_f = 10^{-10}$ Pa⁻¹, and $\beta_f = 2 \times 10^{-11}$ Pa⁻¹ (*54*).Using the above information, we estimate a permeability of 6.0×10^{-17}m².
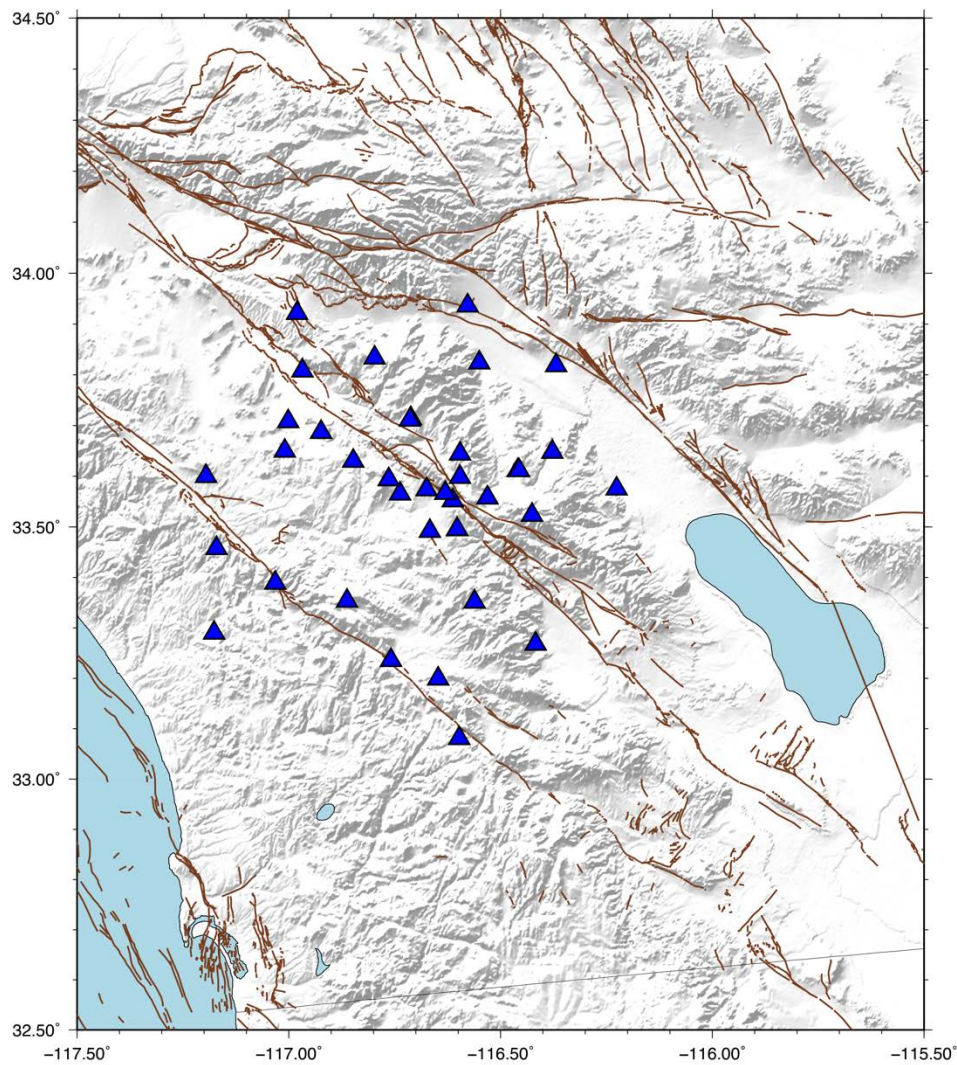
Fig. S1.

Map of region used to generate training dataset for PhaseLink algorithm. Blue triangles indicate station distribution used. Synthetic earthquake hypocenters are placed randomly throughout the region to produce a dataset of arrival times for training (see methods).
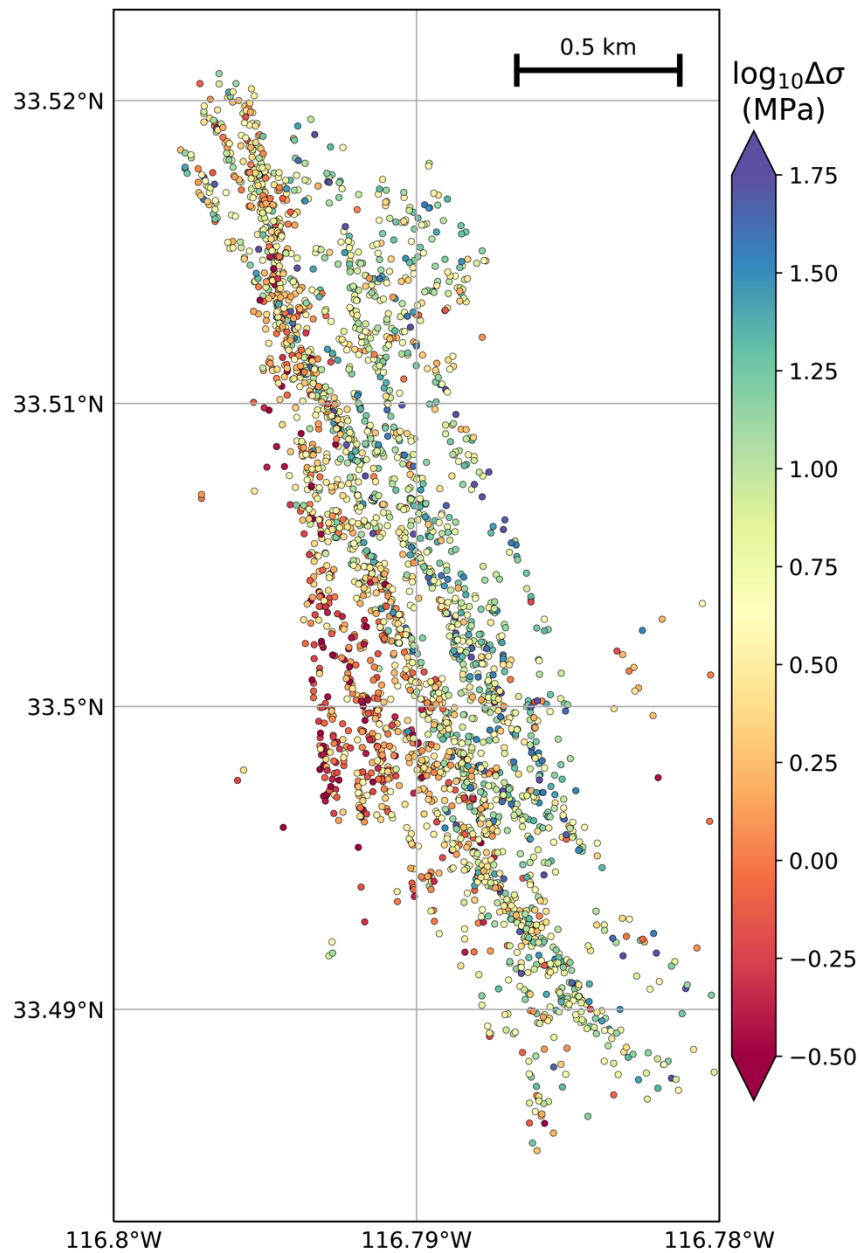
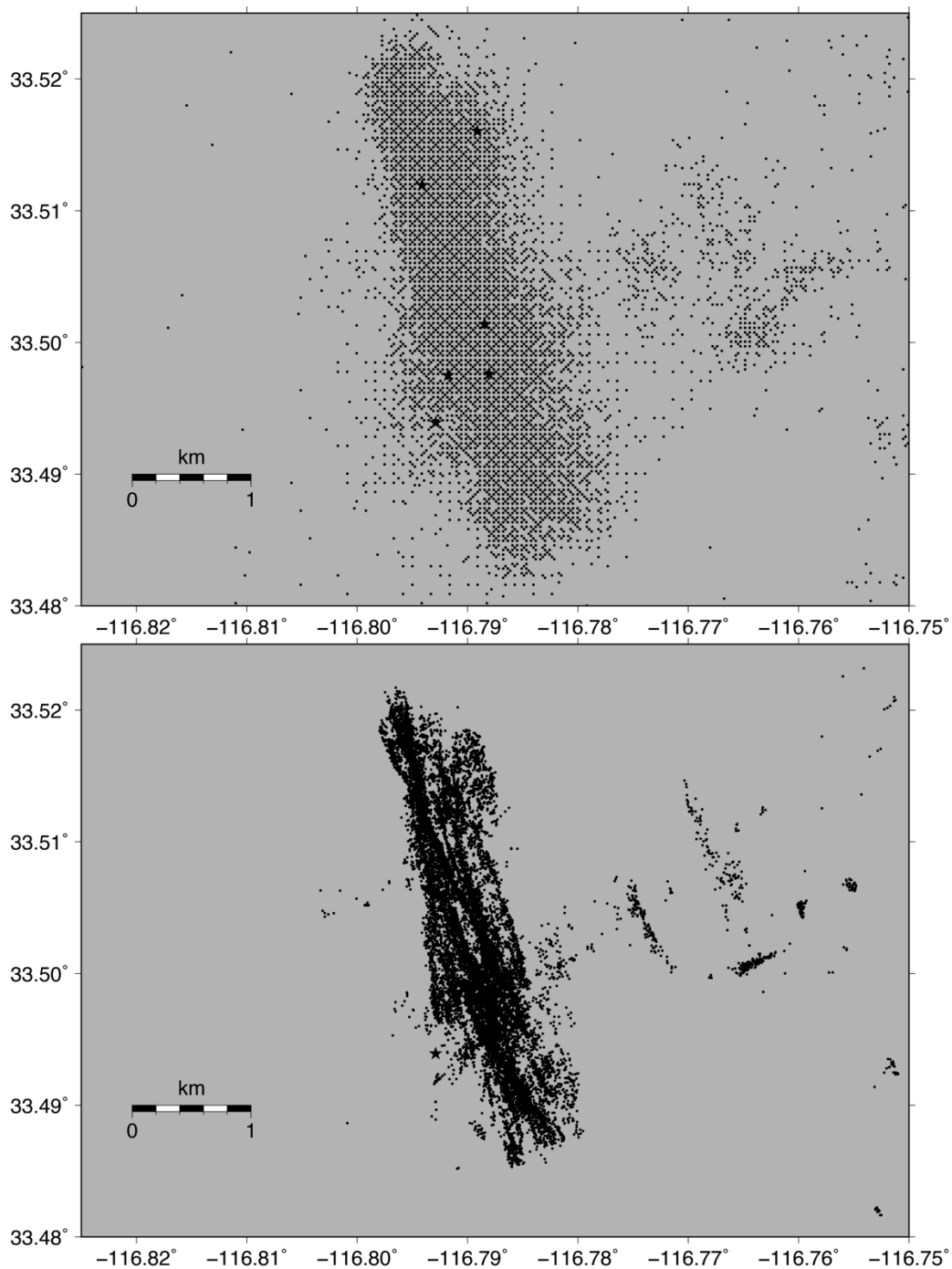**Fig. S2.**
Map of stress drops for the entire sequence.

Fig. S3.

Seismicity before (upper panel; 22,700 events) and after (lower panel; 20,966 events) relocation with GrowClust.
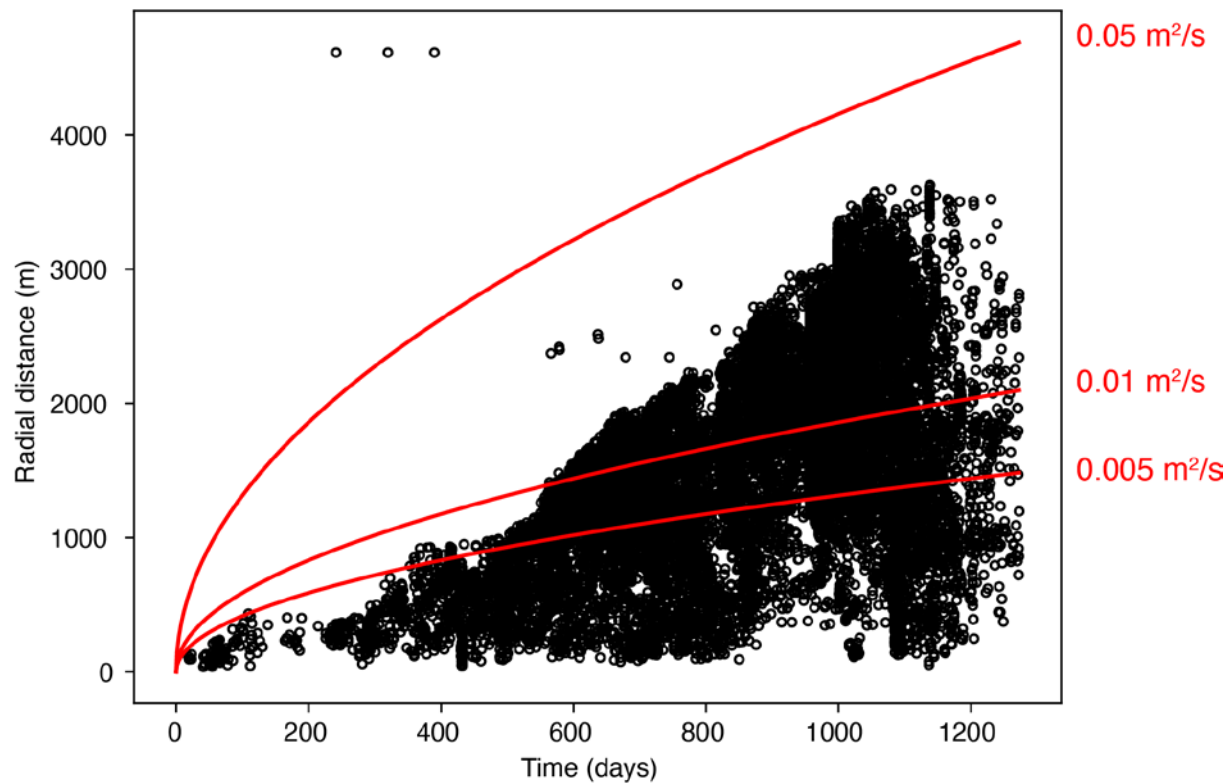
Fig. S4.

Estimating the diffusivity (D) of the Cahuilla swarm. Curves are plotted using the equation $r = \sqrt{4Dt}$, following Talwani et al. (*53*). This figure demonstrates that the sequence is not well-characterized by a square-root of time migration for any value of D.
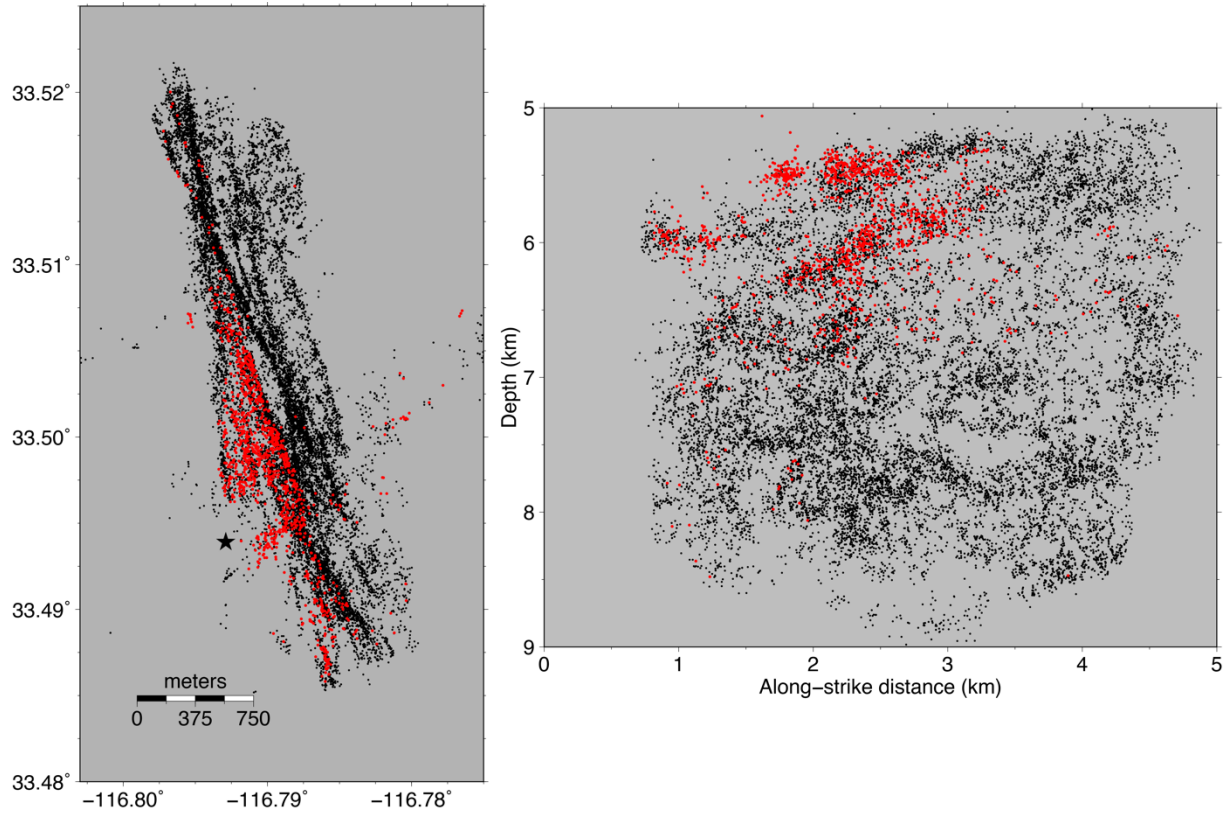
Fig. S5.

Aftershocks of the M4.4 event within 10 days (red dots). Cross section is the same as in Fig. 2 (Z-Z').
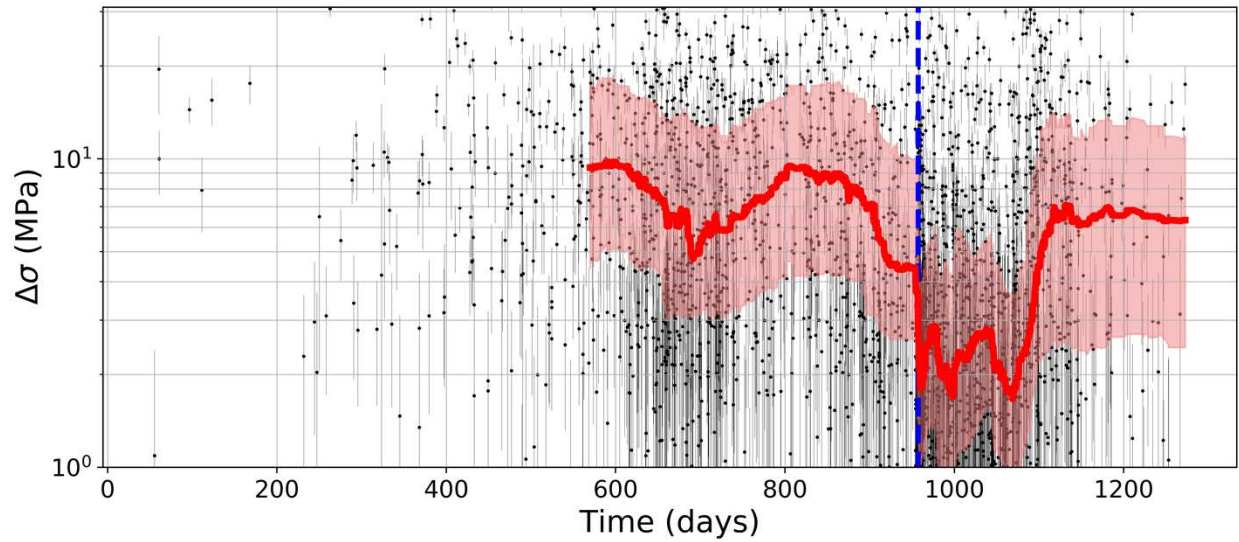
Fig. S6.

Time evolution of stress drop ($\Delta\sigma$). Solid red line marks the median $\Delta\sigma$ in a causal, 200-event moving window. Shading denotes inter-quartile range. Similar to Fig. 3a in the main text, but with 1-sigma uncertainty error bars shown for each event, obtained from a bootstrap resampling over the stations that go into each source spectral measurement.

References and Notes

1. J. E. Vidale, P. M. Shearer, A survey of 71 earthquake bursts across southern California: Exploring the role of pore fluid pressure fluctuations and aseismic slip as drivers. *J. Geophys. Res.* **111**, 12 (2006). [doi:10.1029/2005JB004034](doi:10.1029/2005JB004034)

2. I. Zaliapin, Y. Ben-Zion, Earthquake clusters in southern California II: Classification and relation to physical properties of the crust. *J. Geophys. Res.* **118**, 2865–2877 (2013). doi:10.1002/jgrb.50178

3. E. Roland, J. J. McGuire, Earthquake swarms on transform faults. *Geophys. J. Int.* **178**, 1677–1690 (2009). [doi:10.1111/j.1365-246X.2009.04214.x](doi:10.1111/j.1365-246X.2009.04214.x)

4. S. Hainzl, T. Fischer, H. Čermáková, M. Bachura, J. Vlček, Aftershocks triggered by fluid intrusion: Evidence for the aftershock sequence occurred 2014 in West Bohemia/Vogtland. *J. Geophys. Res.* **121**, 2575–2590 (2016). [doi:10.1002/2015JB012582](doi:10.1002/2015JB012582)

5. S. A. Miller, C. Collettini, L. Chiaraluce, M. Cocco, M. Barchi, B. J. P. Kaus, Aftershocks driven by a high-pressure CO2 source at depth. *Nature* **427**, 724–727 (2004). doi:10.1038/nature02251 Medline

6. X. Chen, P. M. Shearer, Comprehensive analysis of earthquake source spectra and swarms in the Salton Trough, California. *J. Geophys. Res.* **116**, B09309 (2011). [doi:10.1029/2011JB008263](doi:10.1029/2011JB008263)

7. F. M. Chester, J. S. Chester, Ultracataclasite structure and friction processes of the Punchbowl fault, San Andreas system, California. *Tectonophysics* **295**, 199–221 (1998). [doi:10.1016/S0040-1951(98)00121-8](doi:10.1016/S0040-1951(98)00121-8)

8. T. M. Mitchell, D. R. Faulkner, The nature and origin of off-fault damage surrounding strike-slip fault zones with a wide range of displacements: A field study from the Atacama fault system, northern Chile. *J. Struct. Geol.* **31**, 802–816 (2009). [doi:10.1016/j.jsg.2009.05.002](doi:10.1016/j.jsg.2009.05.002)

9. Y. Ben-Zion, C. G. Sammis, Characterization of Fault Zones. *Pure Appl. Geophys.* **160**, 677–715 (2003). [doi:10.1007/PL00012554](doi:10.1007/PL00012554)

10. J. S. Caine, J. P. Evans, C. B. Forster, Fault zone architecture and permeability structure. *Geology* **24**, 1025–1028 (1996). doi:10.1130/0091-7613(1996)024<1025:FZAAPS>2.3.CO;2

11. V. F. Bense, T. Gleeson, S. E. Loveless, O. Bour, J. Scibek, Fault zone hydrogeology. *Earth Sci. Rev.* **127**, 171–192 (2013). doi:10.1016/j.earscirev.2013.09.008

12. V. F. Bense, M. A. Person, Faults as conduit-barrier systems to fluid flow in siliciclastic sedimentary aquifers. *Water Resour. Res.* **42**, W05421 (2006). [doi:10.1029/2005WR004480](doi:10.1029/2005WR004480)

13. M. Manga, I. Beresnev, E. E. Brodsky, J. E. Elkhoury, D. Elsworth, S. E. Ingebritsen, D. C. Mays, C.-Y. Wang, Changes in permeability caused by transient stresses: Field observations, experiments, and mechanisms. *Rev. Geophys.* **50**, RG2004 (2012). [doi:10.1029/2011RG000382](doi:10.1029/2011RG000382)

14. L. Xue, H.-B. Li, E. E. Brodsky, Z.-Q. Xu, Y. Kano, H. Wang, J. J. Mori, J.-L. Si, J.-L. Pei, W. Zhang, G. Yang, Z.-M. Sun, Y. Huang, Continuous permeability measurements record healing inside the Wenchuan earthquake fault zone. *Science* **340**, 1555–1559 (2013). doi:10.1126/science.1237237 Medline

15. R. H. Sibson, Structural permeability of fluid-driven fault-fracture meshes. *J. Struct. Geol.* **18**, 1031–1042 (1996). [doi:10.1016/0191-8141(96)00032-6](doi:10.1016/0191-8141(96)00032-6)

16. D. R. Faulkner, A. C. Lewis, E. H. Rutter, On the internal structure and mechanics of large strike-slip fault zones: Field observations of the Carboneras fault in southeastern Spain. *Tectonophysics* **367**, 235–251 (2003). [doi:10.1016/S0040-1951(03)00134-3](doi:10.1016/S0040-1951(03)00134-3)

17. F. M. Chester, C. Rowe, K. Ujiie, J. Kirkpatrick, C. Regalla, F. Remitti, J. C. Moore, V. Toy, M. Wolfson-Schwehr, S. Bose, J. Kameda, J. J. Mori, E. E. Brodsky, N. Eguchi, S. Toczko; Expedition 343 and 343T Scientists, Structure and composition of the plate-boundary slip zone for the 2011 Tohoku-Oki earthquake. *Science* **342**, 1208–1211 (2013). doi:10.1126/science.1243719 Medline

18. V. Heesakkers, S. Murphy, Z. Reches, Earthquake Rupture at Focal Depth, Part I: Structure and Rupture of the Pretorius Fault, TauTona Mine, South Africa. *Pure Appl. Geophys.* **168**, 2395–2425 (2011). [doi:10.1007/s00024-011-0354-7](doi:10.1007/s00024-011-0354-7)

19. D. R. Shelly, W. L. Ellsworth, D. P. Hill, Fluid-faulting evolution in high definition: Connecting fault structure and frequency-magnitude variations during the 2014 Long Valley Caldera, California, earthquake swarm. *J. Geophys. Res.* **121**, 1776–1795 (2016). [doi:10.1002/2015JB012719](doi:10.1002/2015JB012719)

20. A. A. Allam, Y. Ben-Zion, Seismic velocity structures in the southern California plate-boundary environment from double-difference tomography. *Geophys. J. Int.* **190**, 1181–1196 (2012). [doi:10.1111/j.1365-246X.2012.05544.x](doi:10.1111/j.1365-246X.2012.05544.x)

21. S. J. Wei, E. Fielding, S. Leprince, A. Sladen, J. P. Avouac, D. Helmberger, E. Hauksson, R. S. Chu, M. Simons, K. Hudnut, T. Herring, R. Briggs, Superficial simplicity of the 2010 El Mayor-Cucapah earthquake of Baja California in Mexico. *Nat. Geosci.* **4**, 615–618 (2011). doi:10.1038/ngeo1213

22. Z. E. Ross, B. Idini, Z. Jia, O. L. Stephenson, M. Zhong, X. Wang, Z. Zhan, M. Simons, E. J. Fielding, S.-H. Yun, E. Hauksson, A. W. Moore, Z. Liu, J. Jung, Hierarchical interlocked orthogonal faulting in the 2019 Ridgecrest earthquake sequence. *Science* **366**, 346–351 (2019). doi:10.1126/science.aaz0109 Medline

23. Z. E. Ross, E. Hauksson, Y. Ben-Zion, Abundant off-fault seismicity and orthogonal structures in the San Jacinto fault zone. *Sci. Adv.* **3**, e1601946 (2017). doi:10.1126/sciadv.1601946 Medline

24. E. Hauksson, Z. E. Ross, E. Cochran, Slow-Growing and Extended-Duration Seismicity Swarms: Reactivating Joints or Foliations in the Cahuilla Valley Pluton, Central Peninsular Ranges, Southern California. *J. Geophys. Res.* **124**, 3933–3949 (2019). [doi:10.1029/2019JB017494](doi:10.1029/2019JB017494)

25. R. V. Sharp, San Jacinto Fault Zone in the Peninsular Ranges of Southern California. *Bull. Geol. Soc. Am.* **78**, 705–730 (1967). [doi:10.1130/0016-7606(1967)78[705:SJFZIT]2.0.CO;2](doi:10.1130/0016-7606(1967)78[705:SJFZIT]2.0.CO;2)

26. Materials and methods are described in the supplementary materials.

27. S. A. Shapiro, P. Audigane, J.-J. Royer, Large-scale in situ permeability tensor of rocks from induced microseismicity. *Geophys. J. Int.* **137**, 207–213 (1999). doi:10.1046/j.1365-246x.1999.00781.x

28. S. Hainzl, Y. Ogata, Detecting fluid signals in seismicity data through statistical earthquake modeling. *J. Geophys. Res.* **110**, B05S07 (2005). doi:10.1029/2004JB003247

29. S. F. Cox, Injection-Driven Swarm Seismicity and Permeability Enhancement: Implications for the Dynamics of Hydrothermal Ore Systems in High Fluid-Flux, Overpressured Faulting Regimes—An Invited Paper. *Econ. Geol.* **111**, 559–587 (2016). doi:10.2113/econgeo.111.3.559

30. H. Kanamori, L. Rivera, in *Earthquakes: Radiated Energy and the Physics of Faulting*, R. Abercrombie, A. McGarr, G. D. Toro, H. Kanamori, Eds. (American Geophysical Union, 2006), pp. 3–13.

31. N. E. Odling, S. D. Harris, R. J. Knipe, Permeability scaling properties of fault damage zones in siliclastic rocks. *J. Struct. Geol.* **26**, 1727–1747 (2004). doi:10.1016/j.jsg.2004.02.005

32. S. Brown, A. Caprihan, R. Hardy, Experimental observation of fluid flow channels in a single fracture. *J. Geophys. Res.* **103**, 5125–5132 (1998). doi:10.1029/97JB03542

33. W. L. Power, T. E. Tullis, S. R. Brown, G. N. Boitnott, C. H. Scholz, Roughness of natural fault surfaces. *Geophys. Res. Lett.* **14**, 29–32 (1987). doi:10.1029/GL014i001p00029

34. R. H. Sibson, "Fluid flow accompanying faulting: Field evidence and models" in *Earthquake Prediction: An International Review*, vol. 4, D. W. Simpson, P. G. Richards, Eds. (American Geophysical Union, 1981), pp. 593–603.

35. R. H. Sibson, An episode of fault-valve behaviour during compressional inversion?— The 2004 MJ6.8 Mid-Niigata Prefecture, Japan, earthquake sequence. *Earth Planet. Sci. Lett.* **257**, 188–199 (2007). doi:10.1016/j.epsl.2007.02.031

36. J. M. Gosselin, P. Audet, C. Estève, M. McLellan, S. G. Mosher, A. J. Schaeffer, Seismic evidence for megathrust fault-valve behavior during episodic tremor and slip. *Sci. Adv.* **6**, eaay5174 (2020). doi:10.1126/sciadv.aay5174 Medline

37. P. M. Shearer, G. A. Prieto, E. Hauksson, Comprehensive analysis of earthquake source spectra in southern California. *J. Geophys. Res.* **111**, B06303 (2006). doi:10.1029/2005JB003979

38. California Institute of Technology Dataset, Southern California Earthquake Data Center (2013); doi:10.7909/C3WD3xH1

39. Z. E. Ross, M.-A. Meier, E. Hauksson, T. H. Heaton, Generalized Seismic Phase Detection with Deep Learning. *Bull. Seismol. Soc. Am.* **108**, 2894–2901 (2018). doi:10.1785/0120180080

40. O. Ronneberger, P. Fischer, T. Brox, in *Medical Image Computing and Computer-Assisted Intervention – MICCAI 2015*, of *Lecture Notes in Computer Science*, N. Navab, J. Hornegger, W. M. Wells, A. F. Frangi, Eds. (Springer, 2015), pp. 234–241.

41. E. Pardo, C. Garfias, N. Malpica, Seismic Phase Picking Using Convolutional Networks. *IEEE Trans. Geosci. Remote Sens.* **57**, 7086–7092 (2019). doi:10.1109/TGRS.2019.2911402

42. D. P. Kingma, J. Ba, Adam: A Method for Stochastic Optimization. arXiv:14126980 [cs.LG] (22 Dec 2014).

43. Z. E. Ross, Y. Yue, M.-A. Meier, E. Hauksson, T. H. Heaton, PhaseLink: A Deep Learning Approach to Seismic Phase Association. *J. Geophys. Res.* **124**, 856–869 (2019). doi:10.1029/2018JB016674

44. A. Lomax, J. Virieux, P. Volant, C. Berge-Thierry, in *Advances in Seismic Event Location*, of *Modern Approaches in Geophysics*, C. H. Thurber, N. Rabinowitz, Eds. (Springer, 2000), pp. 101–134.

45. D. Hadley, H. Kanamori, Seismic structure of the Transverse Ranges, California. *Bull. Geol. Soc. Am.* **88**, 1469–1478 (1977). doi:10.1130/0016-7606(1977)88<1469:SSOTTR>2.0.CO;2

46. R. A. Uhrhammer, M. Hellweg, K. Hutton, P. Lombard, A. W. Walters, E. Hauksson, D. Oppenheimer, California Integrated Seismic Network (CISN) Local Magnitude Determination in California and Vicinity. *Bull. Seismol. Soc. Am.* **101**, 2685–2693 (2011). doi:10.1785/0120100106

47. S. Wiemer, M. Wyss, Minimum Magnitude of Completeness in Earthquake Catalogs: Examples from Alaska, the Western United States, and Japan. *Bull. Seismol. Soc. Am.* **90**, 859–869 (2000). doi:10.1785/0119990114

48. D. T. Trugman, P. M. Shearer, GrowClust: A Hierarchical Clustering Algorithm for Relative Earthquake Relocation, with Application to the Spanish Springs and Sheldon, Nevada, Earthquake Sequences. *Seismol. Res. Lett.* **88**, 379–391 (2017). doi:10.1785/0220160188

49. D. T. Trugman, S. L. Dougherty, E. S. Cochran, P. M. Shearer, Source Spectral Properties of Small to Moderate Earthquakes in Southern Kansas. *J. Geophys. Res.* **122**, 8021–8034 (2017). doi:10.1002/2017JB014649

50. J. N. Brune, Tectonic stress and the spectra of seismic shear waves from earthquakes. *J. Geophys. Res.* **75**, 4997–5009 (1970). doi:10.1029/JB075i026p04997

51. Y. Kaneko, P. M. Shearer, Seismic source spectra and estimated stress drop derived from cohesive-zone models of circular subshear rupture. *Geophys. J. Int.* **197**, 1002–1015 (2014). doi:10.1093/gji/ggu030

52. S. A. Shapiro, E. Huenges, G. Borm, Estimating the crust permeability from fluid-injection-induced seismic emission at the KTB site. *Geophys. J. Int.* **131**, F15–F18 (1997). doi:10.1111/j.1365-246X.1997.tb01215.x

53. P. Talwani, L. Chen, K. Gahalaut, Seismogenic permeability, k_s. *J. Geophys. Res.* **112**, B07309 (2007). doi:10.1029/2006JB004665

54. P. Talwani, J. S. Cobb, M. F. Schaeffer, In situ measurements of hydraulic properties of a shear zone in northwestern South Carolina. *J. Geophys. Res.* **104**, 14993–15003 (1999). doi:10.1029/1999JB900059